Research Square

Preprints are preliminary reports that have not undergone peer review.
They should not be considered conclusive, used to inform clinical practice,
or referenced by the media as validated information.

Deep Learning-Based Prediction of SAR and Ein in the Human Head Exposed to Mobile Phone Electromagnetic Radiation

Rui Tian

tianrui@Lzjtu.edu.cn

Lanzhou Jiaotong University

Rui Zhang

Lanzhou Jiaotong University

Juchuan Wei

Lanzhou Jiaotong University

Mai Lu

Lanzhou Jiaotong University

Article

Keywords: Electromagnetic exposure, SAR, Ein, Human head model, 3D U-Net

Posted Date: November 25th, 2026

DOI: https://doi.org/10.21203/rs.3.rs-11759522/v1

License: This work is licensed under a Creative Commons Attribution 4.0 International License.
Read Full License

Additional Declarations: No competing interests reported.

Deep Learning-Based Prediction of SAR and E_{in} in the Human Head Exposed to Mobile Phone Electromagnetic Radiation

Rui Tian[a,b,*], Rui Zhang[a,b], Juchuan Wei[a,c], Mai Lu[a]

[a] Key Laboratory of Opto-Electronic Technology and Intelligent Control of Ministry of Education, Lanzhou Jiaotong University, Lanzhou 730070, China

[b] School of Electronic and Information Engineering, Lanzhou Jiaotong University, Lanzhou 730070, China

[c] School of Automation and Electrical Engineering, Lanzhou Jiaotong University, Lanzhou 730070, China

*Corresponding author: Rui Tian (1977–), female, Han Chinese, born in Lanzhou, Gansu, China. Ph.D. Professor Research interests: intelligent electromagnetic computing, bioelectromagnetic dosimetry. E-mail: tianrui@Lzjtu.edu.cn.

Funding: National Natural Science Foundation of China (Grant No. 62361035).

Abstract: Mobile phones generate electromagnetic fields during operation, exposing the human head to electromagnetic radiation. Traditional numerical methods are complex and computationally expensive, limiting rapid exposure assessment. This study proposes a 3D U-Net incorporating physics-aware spatial encoding and a Convolutional Block Attention Module (CBAM) for efficient, flexible assessment of head electromagnetic exposure. First, 3D electromagnetic finite element models of the human head and mobile phone were established. By varying their relative spatial positions, initial 3D point cloud data of SAR_{10g} and induced electric field (E_{in}) were obtained. Different padding strategies (zero, first-row , and circular padding) were then applied, and the head–phone spatial positions were encoded using physics-aware features. Finally, datasets with different physics-aware encoding methods (6 and 8 channels) trained the 3D CBAM U-Net to determine the optimal network configuration. Results show that zero padding combined with 8-channel physics-aware spatial encoding achieved the best performance, with average relative errors of 0.748% for SAR_{10g} and 1.523% for E_{in}. Each prediction took only 0.57 s，approximately 51 times faster than the finite-element simulation. The proposed method learns the mapping between phone configurations and electromagnetic responses in the human head, reduces assessment time, and provides an efficient, accurate, generalizable approach.

Keywords: Electromagnetic exposure, SAR, E_{in}, Human head model, 3D U-Net.

Introduction

Electromagnetic fields are invisible, odorless, and imperceptible, allowing them to persist in the environment and potentially affect human health without direct awareness[1-2]. ICNIRP[3] and IEEE C95.1[4] are based on established acute health effects and provide scientific recommendations to protect humans from the adverse effects of non-ionizing radiation. In China, the Environmental Code of the People's Republic of China, which came into force on August 15, 2026, includes a dedicated chapter on the prevention and control of electromagnetic radiation pollution and imposes higher requirements for electromagnetic radiation from mobile terminals[5].

Smartphones have become one of the most widely used mobile devices in daily life[6]. During mobile phone use, users may adopt various holding postures, such as placing the earpiece directly against the ear or holding the phone at a certain distance from the ear. This leads to random variations in the distance and orientation of the RF source relative to the head, consequently altering the electromagnetic exposure level of the head[7-8]. Traditional approaches for electromagnetic exposure assessment primarily include experimental measurements[9-10], epidemiological investigations[11] and numerical electromagnetic simulations[12]. Among these approaches, numerical simulations can accurately characterize complex electromagnetic propagation processes and outcomes, and have become an important technique for electromagnetic field analysis[13-14]. However, under multi-scenario and multi-parameter coupling conditions, this approach cannot predict electromagnetic field distributions in untested scenarios based on existing simulation results. Moreover, its high computational cost and long computation time limit its suitability for

rapid RF electromagnetic exposure assessment across multiple scenarios[15].

In recent years, deep learning-based surrogate models, leveraging their advantages in nonlinear mapping and data-driven learning, have given rise to a new field of intelligent electromagnetic computation[16-17]. Researchers have applied them to problems such as antenna design and magnetic field distribution prediction. To address this issue, the basic strategy is to first obtain a limited number of simulation results using numerical methods and construct a dataset. Then, deep learning models are trained and tested, enabling the network model to effectively simulate the numerical computation process of a specific field. A convolutional neural network model was developed to achieve rapid prediction of antenna distributions and electromagnetic responses[18]. Machine learning and deep learning models have also been used to estimate electromagnetic field exposure levels at specific locations in urban environments[19]. In addition, an artificial neural network (ANN) combined with feature extraction and selection was employed to predict electromagnetic field exposure levels in urban environments[20]. Classical electromagnetic algorithms have been combined with deep learning to evaluate the incident power density of wireless communication devices operating above 6 GHz[21]. Reference [22] proposed a multi-channel three-dimensional convolutional neural network (3D CNN) model to predict the local SAR distribution in the human head for a 7T magnetic resonance parallel transmission (pTx) system[22]. Moreover, deep learning has also been applied to rapidly predict TMS-induced electric fields based on MRI images and coil parameters. The results showed that this method can significantly improve computational efficiency[23]. Although previous studies have demonstrated the feasibility of using deep learning to rapidly predict complex electromagnetic responses[24-25], rapid and flexible assessment of RF electromagnetic exposure at multiple locations within the human head due to mobile phone antenna radiation remains challenging.

To address the above issues, this study combines finite element simulations with deep learning to develop a 3D U-Net model that integrates physics-aware spatial encoding inputs and an embedded CBAM[26-27]. The proposed model is used to accurately and efficiently predict SAR_{10g} and E_{in} distributions in the human head, and to assess the effects of mobile phone radiation on the human head. The framework of this study is illustrated in Fig. 1.

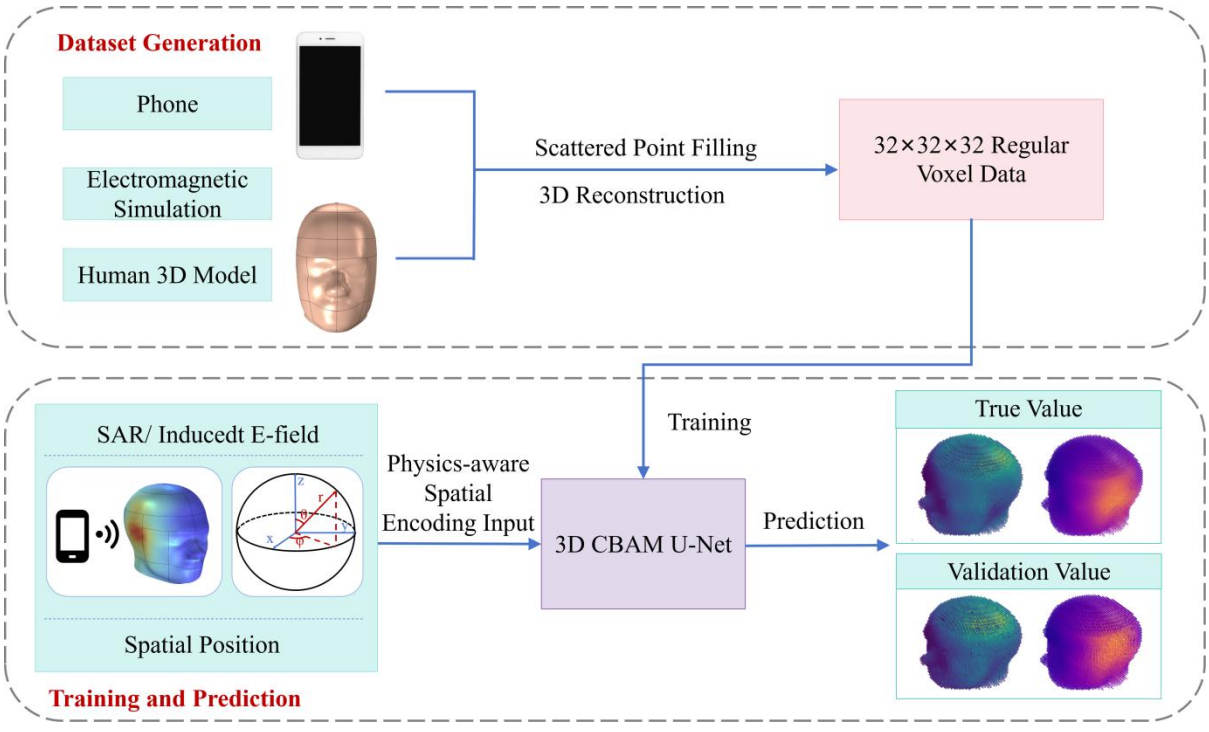

Fig. 1. Technical Roadmap.

Methods

Geometric Model and Electromagnetic Governing Equations

The E_{in} in the head was described by the Helmholtz equation. The energy deposition in head tissues was characterized by SAR_{10g}. The governing equations were defined according to Eq. (1) and Eq. (2), respectively.

$$\nabla\times\mu^{-1}(\nabla\times\boldsymbol{E})\text{-}k_0^2\left(\varepsilon_r\text{-j}\frac{\sigma}{\omega\varepsilon_0}\right)\boldsymbol{E}=0 \quad (1)$$

$$\mathrm{SAR}=\frac{\sigma|\boldsymbol{E}|^2}{2\rho} \quad (2)$$

$\boldsymbol{E}$ denotes the electric field intensity (V/m). $\nabla\times$ is the curl operator, μ is the magnetic permeability (H/m), k_0 is the free-space wavenumber (rad/m), ε_r is the relative permittivity, j is the imaginary unit, σ is the electrical conductivity (S/m), ω is the angular frequency (rad/s), ε_0 is the vacuum permittivity (F/m), ρ is the tissue mass density (kg/m³).

The electrical conductivity and relative permittivity of head tissues are presented in Table 1[28-29]. To simulate the radiation exposure of the human body from a mobile phone WiFi antenna under realistic usage conditions, the mobile phone was placed near the head model. A human head and a mobile phone antenna model were established in the spherical coordinate system. The center of the head was set as the origin of the coordinate system, and the position of the mobile phone was represented by (r, θ, φ). A perfectly matched layer with a thickness of 0.05 m was applied outside the model as the scattering boundary condition (Eq. (3)). A continuity boundary condition was applied at the interface between the head and air (Eq. (4)). The operating frequency and input power of the mobile phone antenna were set to 2.45 GHz and 0.1 W, respectively. The complete model and boundary conditions are shown in Fig. 2.

$$\boldsymbol{n}\times(\nabla\times\boldsymbol{E})-\mathrm{j}k\boldsymbol{n}\times(\boldsymbol{E}\times\boldsymbol{n})=0 \quad (3)$$

$$\boldsymbol{n}\times(\boldsymbol{E_1}-\boldsymbol{E_2})=0 \quad \boldsymbol{n}\times(\boldsymbol{H_1}-\boldsymbol{H_2})=0 \quad (4)$$

Table 1 Tissue parameters of the human head at 2.45 GHz

Parameter	Human head
Electrical conductivity σ(S/m)	0.4
Relative permittivity ε_r	11.35
Density ρ（kg/m³）	2000

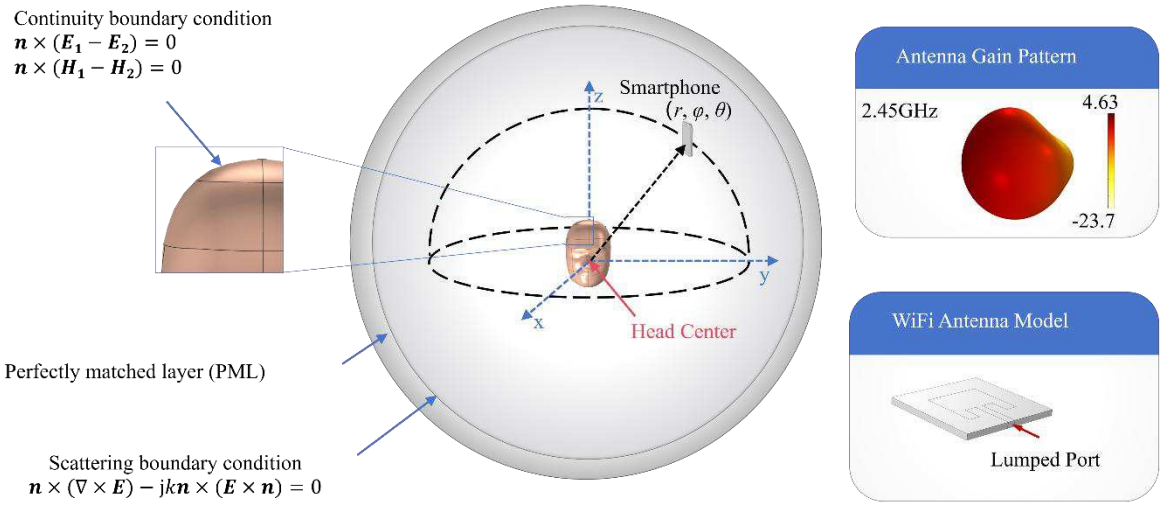

Fig. 2. Geometric model, boundary conditions, and antenna gain diagram.

$\boldsymbol{n}$ is the unit normal vector, $\boldsymbol{E}_1$ and $\boldsymbol{E}_2$ are the electric field intensity vectors in medium 1 and medium 2, respectively, $\boldsymbol{H}_1$ and $\boldsymbol{H}_2$ are the magnetic field intensity vectors in medium 1 and medium 2, respectively, ∇ denotes gradient operator.

3D CBAM U-Net

CBAM consists of the Channel Attention (CA) module and the Spatial Attention (SA) module. The CA module performs global average pooling and global max pooling separately. The channel attention weights are generated through the MLP and Sigmoid activation. The weights are then multiplied with the input feature map channel by channel. The SA module performs average pooling and max pooling along the channel dimension separately. The pooled features are concatenated and fed into a 3D convolution followed by Sigmoid activation to generate spatial attention weights, which are then multiplied with the input feature map element by element. The CBAM structure is shown in Fig. 3.

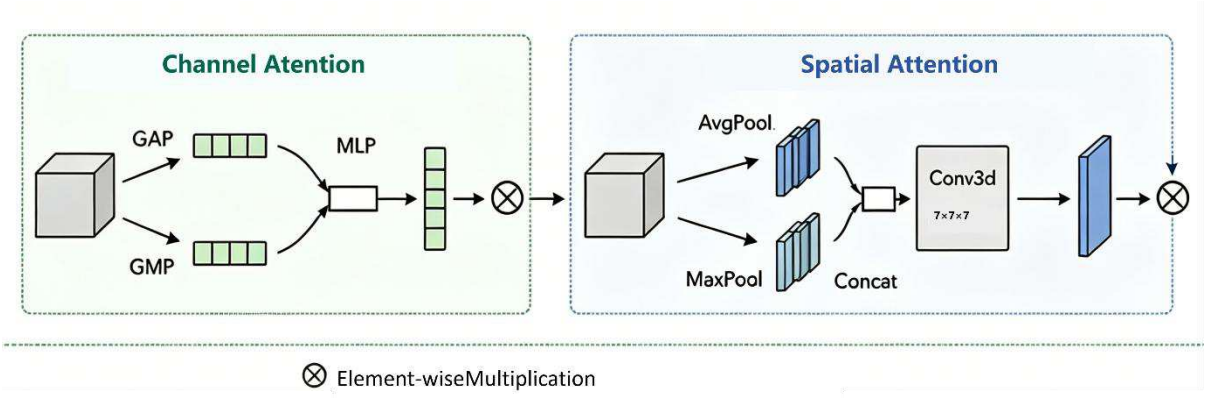

Fig. 3. CBAM.

Traditional U-Net applies equal feature responses to all spatial locations and channels, making it difficult to highlight small structures and limiting its generalization capability across different tasks. To this end, this study proposes to embed CBAM into each convolutional block and the bottleneck layer of the encoder during deep feature extraction through three downsampling operations to enhance the network's response to key regions and important channels, while keeping the decoder architecture unchanged. The decoder retains three upsampling operations and concatenates features from the corresponding encoder layers through skip connections for feature fusion, enabling end-to-end mapping from input to output. The network architecture is shown in Fig. 4. This study employs the LeakyReLU activation function and batch normalization to mitigate vanishing gradients during training, thereby improving model robustness.

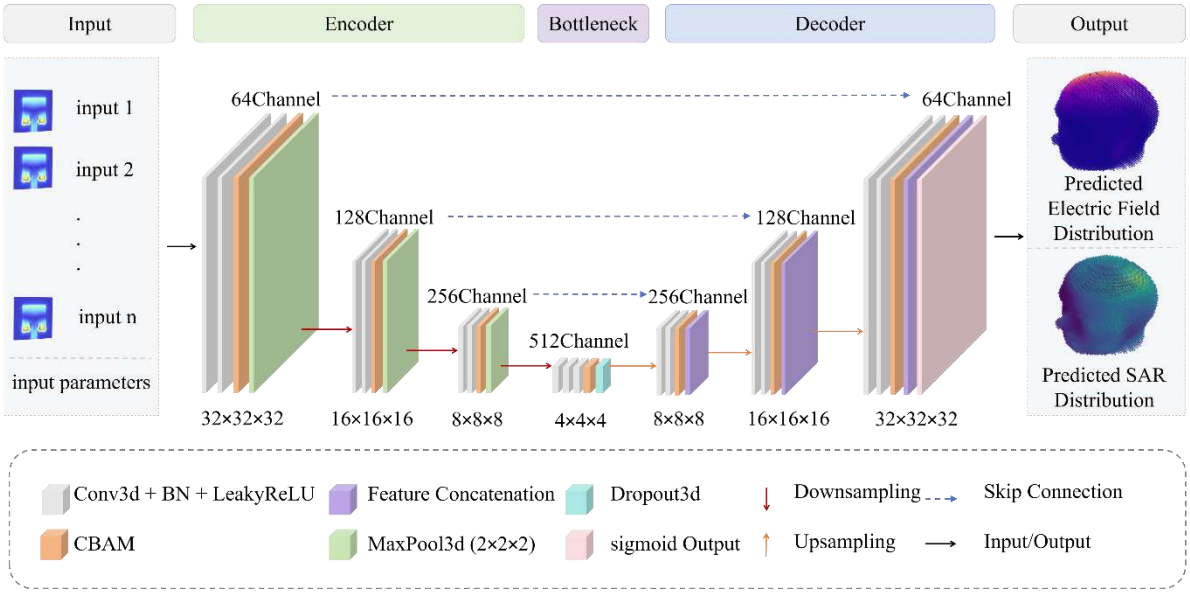

Fig. 4. Architecture of the 3D CBAM U-Net.

Construction of an Electromagnetic Exposure Dataset under Multiple Position Conditions

As shown in Fig. 2, the mobile phone position (r, θ, φ) was varied according to the parameters listed in Table 2. Simulations were performed for all parameter combinations, generating 295 sets of human head SAR_{10g} and E_{in} data. The simulated data were divided into two categories according to the different prediction tasks: head SAR_{10g} data and E_{in} data.

Table 2 Parameter variation ranges

Fixed parameter	Variable parameter	Range	Step	No. of samples
θ=90°	φ	9°–360°	9°	40
φ=90°	θ	0°-81°	9°	10
φ=270°	θ	9°–81°	9°	9
-	r	10–50 mm	10 mm	5

U-Net requires input data to be arranged in a regular cubic grid. However, the head geometry is not cubic, and the point cloud data obtained from finite element simulations are also irregularly distributed. These data cannot directly meet the input requirements of the network. To this end, three filling methods were designed in this study[30-32]. Irregular point cloud data are converted into regular cubic data to meet the input format requirements of the network.

Taking 31,768 SAR_{10g} data points as an example, the data were padded as shown in Table 3. The padded data were then reshaped into a standard 32×32×32 cube to meet the network input requirements. On this basis, the network was trained to evaluate the effects of different padding methods on network stability and prediction accuracy, thereby identifying the optimal padding strategy.

Table 3 Details of Padding Methods

Padding Method	Description	No.
Zero padding	Padding with zero values	I
First-row padding	Padding with the corresponding values from the first row of each data group	II
Circular Padding	Padding with the corresponding values from the first 5% of each data group	III

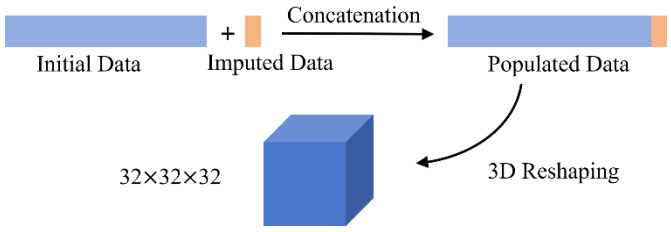

Fig. 5. Data Concatenation Diagram.

Given the pronounced skewness in the distributions of SAR_{10g} and E_{in} values, directly using these data for model training may render the model overly sensitive to high-value regions, thereby compromising its generalization ability. After determining the optimal padding strategy, logarithmic transformation and normalization were applied to the data (Eq. (5) and Eq. (6)) to make the data distribution smoother.

$$x'=\ln(1+x) \quad (5)$$

$$x''=\frac{x'-x_{min}}{x_{max}-x_{min}} \quad (6)$$

where x is the value after imputation, x' is the log-transformed value, x_{min} and x_{max} are the minimum and maximum values after log transformation, respectively, and x'' is the normalized feature value.

Multi-Location Physics-aware Spatial Encoding

To enhance the network's ability to perceive spatial locations, this study proposes a physics-aware spatial encoding method that integrates spatial location information. The encoding is based on three variables

(r, θ, φ) in the spherical coordinate system. Sine and cosine functions are introduced for transformation to construct two encoding schemes with six and eight channels, respectively. The 6-channel encoding consists of $r'\sin\theta'\cos\varphi'$, $r'\sin\theta'\sin\varphi'$, $r'\cos\theta'$, r, θ, and φ. It has a simple structure, but θ and φ exhibit discontinuities at their boundaries. The 8-channel encoding further extends the 6-channel encoding and consists of eight components: $r'\sin\theta'\cos\varphi'$, $r'\sin\theta'\sin\varphi'$, $r'\cos\theta'$, r, $\sin\theta$, $\cos\theta$, $\sin\varphi$, $\cos\varphi$. By applying periodic encoding to the angles, discontinuities at angular boundaries are avoided, allowing the network to capture variations in spatial direction more effectively. In both encoding schemes, the first three channels represent the head position, while the remaining channels represent the position of the smartphone relative to the head.

To evaluate the effects of the two encoding configurations on SAR_{10g} prediction performance, both configurations were trained and tested separately using the same network architecture and training parameters. The results showed that the 8-channel input demonstrated superior capability in learning variations in SAR_{10g} distribution across multiple locations.

Table 4 Physics-Aware Spatial Feature Encoding Method

Encoding Configuration	Number of Channels	Physics-Aware Spatial Feature Encoding
6-channel	6	$r'\sin\theta'\cos\varphi'$, $r'\sin\theta'\sin\varphi'$, $r'\cos\theta'$, r, θ, φ
8-channel	8	$r'\sin\theta'\cos\varphi'$, $r'\sin\theta'\sin\varphi'$, $r'\cos\theta'$, r, $\sin\theta$, $\cos\theta$, $\sin\varphi$, $\cos\varphi$

Loss Function and Evaluation Metrics

To evaluate the suitability of different loss functions for the prediction task, mean absolute error (MAE. Eq. (7)), mean squared error (MSE. Eq. (8)), and Huber loss (Eq. (9)) were compared to quantify the differences between predicted and actual values[33]. In Eqs. (7)–(13), y_i denotes the true value, $\hat{y}_i$ denotes the predicted value, n denotes the total number of voxels, $\bar{y}$ denotes the mean value of the electromagnetic simulation results, and δ denotes the threshold for the Huber loss. During training, the network parameters are updated to minimize the loss function.

$$\mathrm{MAE}=\frac{1}{n}\sum_{i=1}^{n}|y_i-\hat{y}_i| \tag{7}$$

$$\mathrm{MSE}=\frac{1}{n}\sum_{i=1}^{n}(y_i-\hat{y}_i)^2 \tag{8}$$

$$\mathrm{Huber}=\begin{cases}\frac{1}{2}(y_i-\hat{y}_i)^2, & |y_i-\hat{y}_i|\le\delta\\ \delta|y_i-\hat{y}_i|-\frac{1}{2}\delta^2, & |y_i-\hat{y}_i|>\delta\end{cases}\ (\delta=0.1) \tag{9}$$

The mean relative error (Eq. (10)) is used to assess model accuracy. The coefficient of determination ((R^2). Eq. (11)) evaluates how well the model fits the true data. The 3D structural similarity index measure (3D-SSIM. Eq. (12)) assesses consistency between predicted and true data in three-dimensional structure. The root mean square error (RMSE. Eq. (13)) measures the deviation between predicted and true values.

$$\text{Mean Relative Error}=\frac{1}{n}\sum_{i=1}^{n}\left(\frac{|y_i-\hat{y}_i|}{y_i+1}\times 100\%\right) \tag{10}$$

$$R^2=1-\frac{\sum_{i=1}^{n}(y_i-\hat{y}_i)^2}{\sum_{i=1}^{n}(y_i-\bar{y})^2}\quad \bar{y}=\frac{1}{n}\sum_{i=1}^{n}y_i \tag{11}$$

$$\text{3D-SSIM}=\frac{(2\mu_x\mu_y+C_1)(2\sigma_{xy}+C_2)}{(\mu_x^2+\mu_y^2+C_1)(\sigma_x^2+\sigma_y^2+C_2)},\ C_1=(0.01L)^2,\ C_2=(0.03L)^2 \tag{12}$$

$$\mathrm{RMSE}=\sqrt{\frac{1}{n}\sum_{i=1}^{n}(y_i-\hat{y}_i)^2} \qquad (13)$$

Results

The Adam optimizer was used for model training on an NVIDIA GeForce RTX 4060 GPU, using Python 3.8.1 and the PyTorch 1.14.0 framework, with CUDA for GPU acceleration. The model weights were initialized using Kaiming normal initialization. To improve training efficiency and generalization ability, dynamic learning rate adjustment and early stopping strategies were adopted during training. The initial learning rate was set to 0.0001, with a maximum of 300 training epochs. If the validation loss did not decrease for 20 consecutive epochs, the learning rate was reduced to half its previous value. If the validation loss still did not decrease over a longer period (e.g., 100 consecutive epochs), training was terminated early.

Fig. 6 shows the training and validation loss curves for the SAR_{10g} and E_{in} prediction tasks. MAE was used as the loss function for the SAR_{10g} task, while Huber loss was used for the E_{in} task. Both tasks used 8-channel inputs for prediction. The training and validation losses for the head model were 0.006327 and 0.008416, respectively, while those for the E_{in} were 0.000216 and 0.000301, respectively.

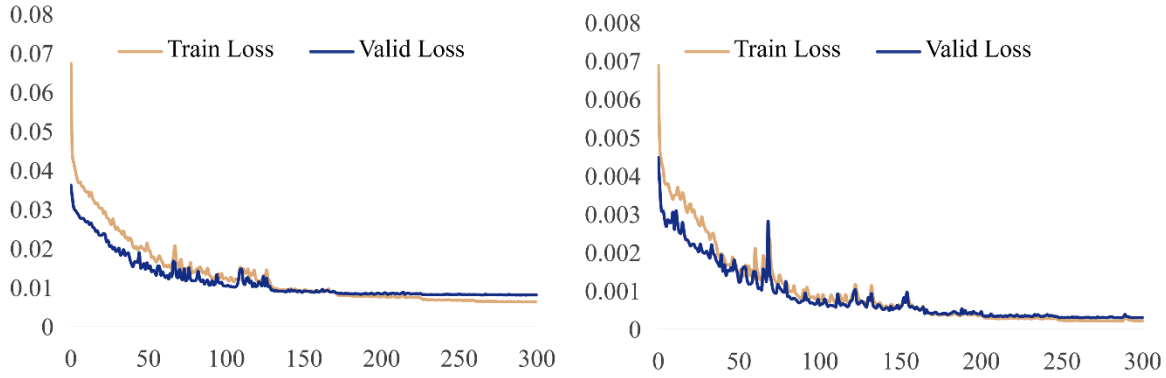

(A)SAR_{10g} **(B)** E_{in}

Fig. 6. Training loss curves.

Fig. 7 As the number of training epochs increased, the mean relative errors for both tasks gradually decreased and stabilized in the later stages of training. The lowest mean relative error was 0.749% for the SAR_{10g} prediction task and 1.523% for the E_{in} prediction task. These results indicate that the model exhibited good convergence stability, with no obvious signs of overfitting.

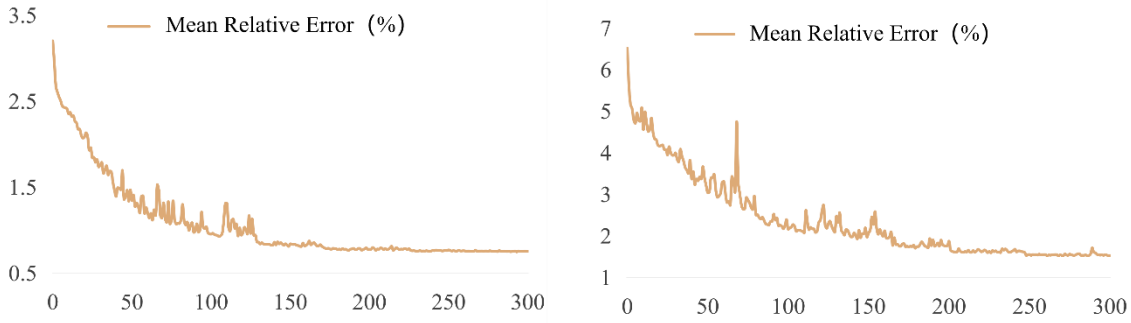

(A)SAR_{10g} **(B)** E_{in}

Fig. 7. Mean relative error curves.

SAR_{10g} Prediction Results

To objectively evaluate the prediction performance of the proposed 3D CBAM U-Net, an independent test set that was not used for training or validation was employed. The surrogate model predictions were compared with the electromagnetic simulation results in terms of prediction error, spatial distribution consistency, and computational efficiency.

Nine parameter combinations were randomly selected outside the original dataset in the order of r-φ-θ (r: 10mm, 30mm, 50mm. φ： 180°, 240°, 300°. θ： 0°, 40°, 80°). The three-dimensional SAR_{10g} distributions at different head locations were predicted and analyzed for errors. The effects of different parameters on head SAR_{10g} were also compared.

At φ=60° and θ=90°, r was set to 10, 30, and 50 mm. The simulated values, predicted values, and absolute errors are shown in Fig. 8. The maximum SAR_{10g} occurred at r=10 mm, with a maximum simulated value of 20.900 mW/kg and a maximum predicted value of 18.800 mW/kg. The maximum absolute error was 2.046 mW/kg. The MAE, RMSE, R^2, and 3D-SSIM for SAR_{10g} were 0.212, 0.391, 0.950, and 0.940, respectively.

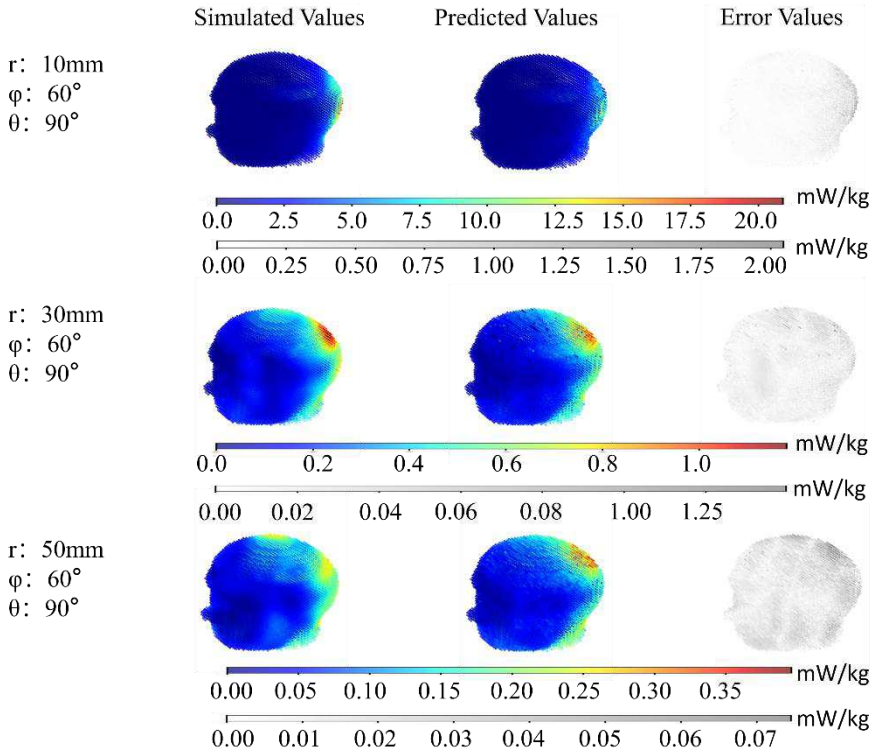

Fig. 8. Comparison of simulated and predicted 3D head SAR_{10g} at different r values.

At r=10 mm and φ=90°, θ was set to 0°, 40°, and 80°. The simulated values, predicted values, and absolute errors are shown in Fig. 9. The maximum SAR_{10g} occurred at θ=0°, with a maximum simulated value of 94.060 mW/kg and a maximum predicted value of 89.870 mW/kg. The maximum absolute error was 4.227 mW/kg. The MAE, RMSE, R^2, and 3D-SSIM for SAR_{10g} were 0.190, 0.489, 0.948, and 0.968, respectively.

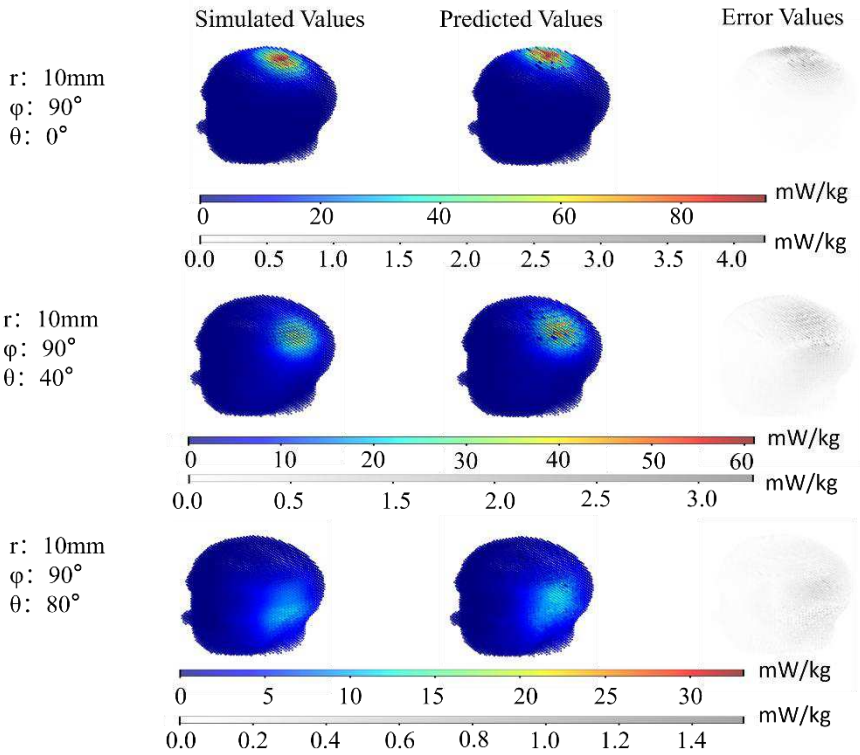

Fig. 9. Comparison of Simulated and Predicted 3D Head SAR_{10g} at Different θ Values.

At r=10mm and θ=90°, φ was set to 180°, 240°, and 300°. The simulated values, predicted values, and absolute errors are shown in Fig. 10. The maximum SAR_{10g} occurred at φ=300°, with a maximum simulated value of 48.230 mW/kg and a maximum predicted value of 46.900 mW/kg. The maximum absolute error was 1.432 mW/kg. The MAE, RMSE, R^2, and 3D-SSIM for SAR_{10g} were 0.169, 0.307, 0.991, and 0.973, respectively.

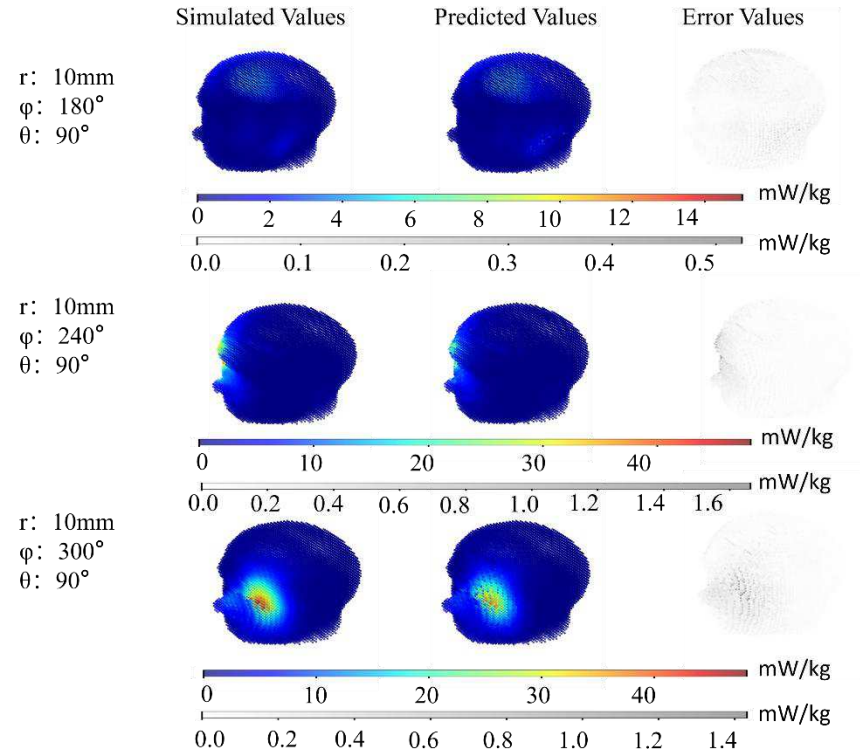

Fig. 10. Comparison of Simulated and Predicted 3D Head SAR_{10g} at Different φ Values.

The prediction results across different combinations of r, φ, and θ show that the model can consistently

and accurately predict the three-dimensional spatial distribution of head SAR_{10g} under different parameter combinations, while maintaining high structural similarity and prediction accuracy. Both the simulated and predicted results are below the 2 W/kg limit specified in the ICNIRP guidelines. In terms of computational efficiency, a single model prediction took 0.57 s, achieving a speedup of approximately 51-fold compared with conventional electromagnetic simulation (approximately 29 s per simulation on average). This indicates that the proposed method can significantly reduce evaluation time while maintaining prediction accuracy. These evaluation metrics demonstrate that the proposed 3D CBAM U-Net model achieves good prediction performance, enabling accurate prediction of SAR_{10g} distributions at different spatial locations and providing a reliable method for rapid assessment of head electromagnetic exposure.

E_{in} Prediction Results

To further evaluate the generalization ability of the 3D CBAM U-Net framework across different electromagnetic response prediction tasks, the network architecture, input feature system, and data processing procedure developed for the SAR_{10g} prediction task were applied to the prediction of three-dimensional E_{in} distributions. In the experiments, the main network architecture and input feature representation remained unchanged. Only the prediction target was changed from the head SAR_{10g} distribution to the E_{in} distribution in the head. The E_{in} distribution exhibits pronounced local gradient variations and unusually high values. The Huber loss function was used to optimize the model for the prediction task, and the model was trained using E_{in} simulation data to improve its generalization ability. Meanwhile, the nine parameter combinations described above were input into the trained model to predict the E_{in} distribution.

At φ=60° and θ=90°, r was set to 10, 30, and 50 mm. The simulated values, predicted values, and absolute errors are shown in Fig. 11. The maximum E_{in} occurred at r=10 mm, with a maximum simulated value of 14.460 V/m and a maximum predicted value of 12.980 V/m. The maximum absolute error was 1.384 V/m. The MAE, RMSE, R^2, and 3D-SSIM for the E_{in} were 0.301, 0.390, 0.962, and 0.974, respectively.

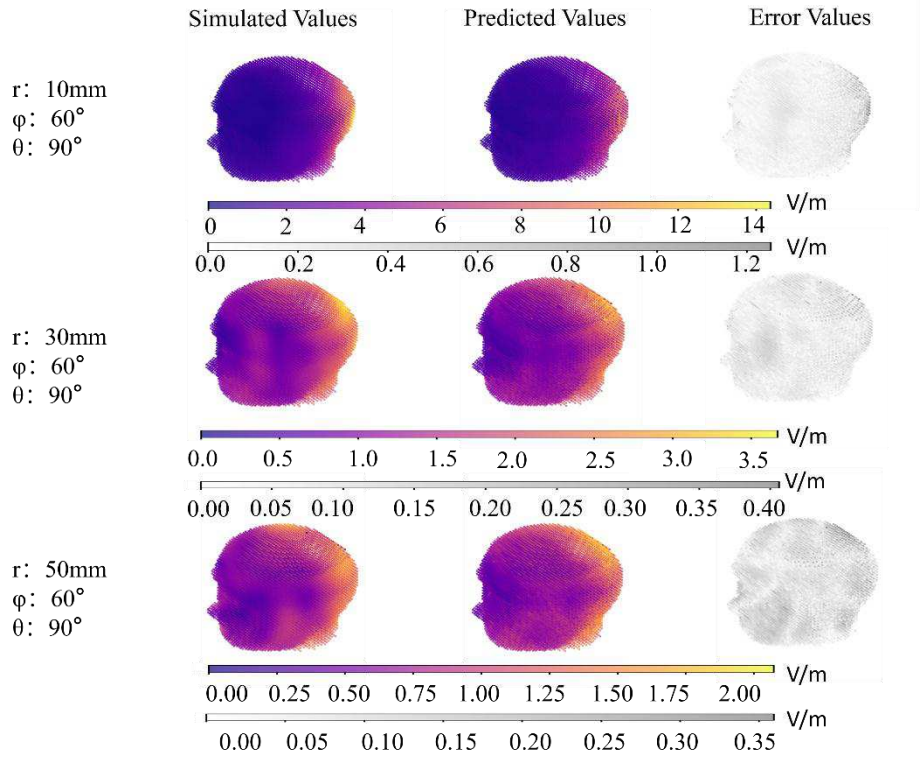

Fig. 11. Comparison of simulated and predicted 3D head E_{in} at different r values.

At r=10 mm and φ=90°, θ was set to 0°, 40°, and 80°. The simulated values, predicted values, and

absolute errors are shown in Fig. 12. The maximum E_{in} value occurred at θ=0°, with a maximum simulated value of 30.670 V/m and a maximum predicted value of 27.000 V/m. The maximum absolute error was 2.120 V/m. The MAE, RMSE, R^2, and 3D-SSIM for the E_{in} were 0.349, 0.485, 0.941, and 0.926, respectively.

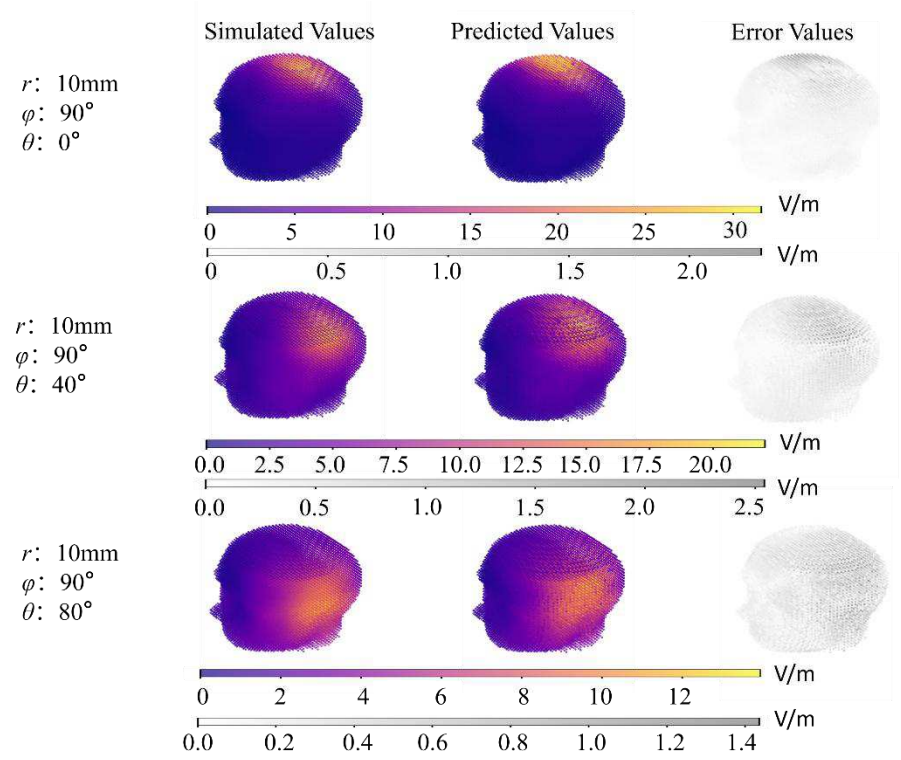

Fig. 12. Comparison of simulated and predicted 3D head E_{in} at different θ values.

At r=10mm and θ=90°, φ was set to 180°, 240°, and 300°. The simulated values, predicted values, and absolute errors are shown in Fig. 13. The maximum E_{in} occurred at φ=300°, with a maximum simulated value of 21.960 V/m and a maximum predicted value of 22.380 V/m. The maximum absolute error was 1.024 V/m. The MAE, RMSE, R^2, and 3D-SSIM for the E_{in} were 0.228, 0.309, 0.988, and 0.988, respectively.

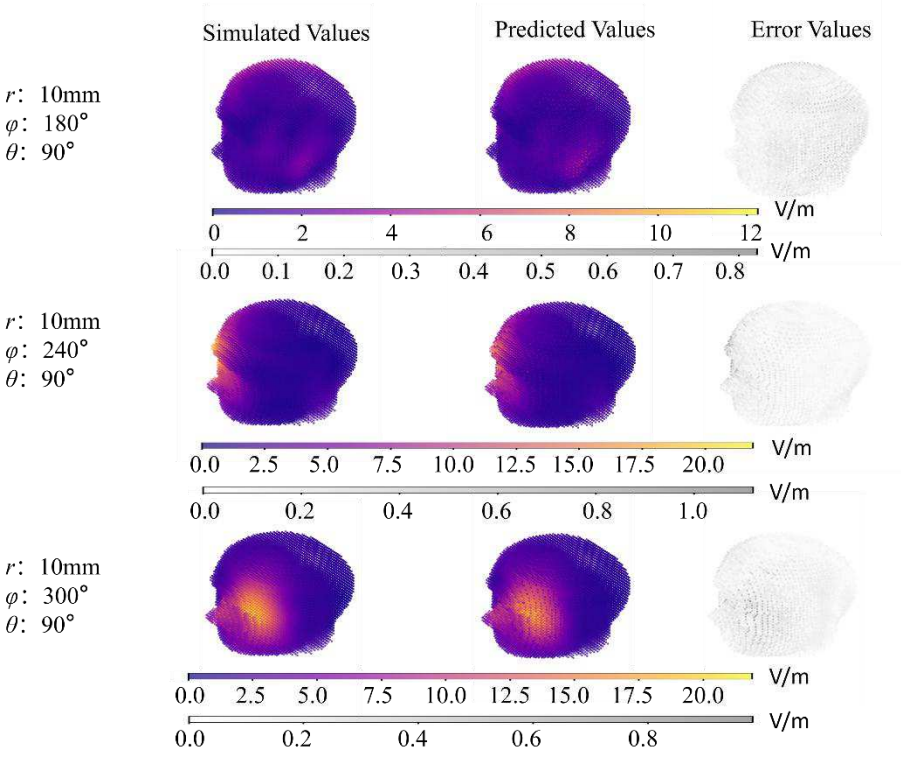

Fig. 13. Comparison of Simulated and Predicted 3D Head E_{in} at Different φ Values.

These results indicate that the 3D CBAM U-Net can adapt to the three-dimensional E_{in} prediction task by adjusting the loss function according to the data distribution characteristics of the target physical quantity and retraining the network, without redesigning the network architecture or modifying the input feature representation. This demonstrates that the proposed model framework has good applicability and task generalization ability across different electromagnetic prediction tasks.

Discussion

Rapid and accurate characterization of the spatial distributions of SAR_{10g} and E_{in} in the human head is essential for assessing RF electromagnetic exposure from mobile phones. To address the need for improved prediction efficiency and flexibility under varying mobile phone positions, this study develops a 3D CBAM U-Net model for rapid prediction. The following analysis focuses on this model. First, the impact of data padding strategies on model performance is investigated. Subsequently, the contributions of physics-aware spatial encoding and the CBAM module are examined. Finally, the reliability of the prediction results is evaluated with reference to the established safety limits.

Analysis of the Effects of Data Padding Strategies on Model Performance

To investigate the effects of data padding strategies and loss functions on SAR_{10g} prediction performance, comparative experiments were conducted on the three data padding strategies (I, II, and III) listed in Table 3, using three loss functions (MAE, MSE, and Huber loss), while keeping the network architecture and training parameters unchanged.

The mean relative error was used as the primary evaluation metric to comprehensively analyze the prediction performance of different padding strategies under each loss function. The experimental results are shown in Fig. 14.

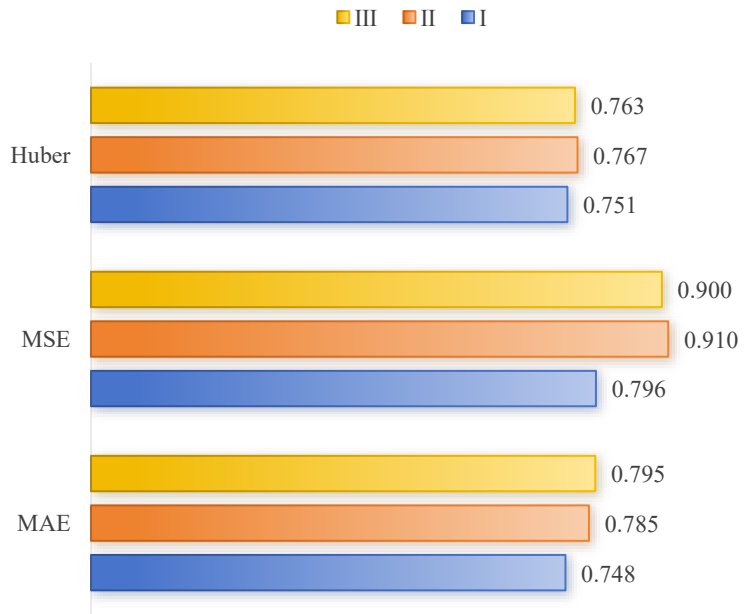

Fig. 14. Comparison of mean relative error (%) under different padding strategies and loss functions

From the perspective of padding strategy, Strategy I achieved the lowest mean relative error under all three loss functions, with values of 0.748%, 0.796%, and 0.751%, respectively, and exhibited the smallest error fluctuation. This indicates that the zero-padding strategy can preserve the spatial continuity of the three-dimensional electromagnetic field, enhance the network's ability to learn electromagnetic features, and

improve prediction stability.

In terms of loss functions, MAE and Huber loss both exhibited consistent stability across different padding strategies. Under Strategy I, Huber loss and MAE yielded similar prediction errors, both outperforming MSE. The mean relative error of MAE was 0.003 percentage points lower than that of Huber loss, indicating that MAE achieved a lower error level while maintaining prediction accuracy. Considering prediction performance, computational complexity, and parameter tuning costs, MAE was selected as the loss function for the SAR_{10g} prediction task.

Analysis of the Impact of Physics-Aware Spatial Encoding on the Model

To evaluate the effects of different physics-aware spatial encoding configurations on SAR_{10g} prediction performance, the model performance with 8-channel and 6-channel physics-aware spatial encoding inputs was compared while keeping the network architecture and training parameters unchanged. The mean relative error was used as the evaluation metric, and the results are shown in Table 5.

Table 5 Comparison of mean relative error (%) under different channels and loss functions

Encoding Configuration	MAE	MSE	Huber	Epoch
6-channels	0.864	0.767	0.939	400
8--channels	0.748	0.796	0.751	300

A comparison of Fig. 15 and Fig. 16 shows that different physics-aware spatial encoding configurations have a significant impact on model prediction performance. The lowest mean relative errors for the 6-channel and 8-channel configurations were 0.767% (MSE) and 0.748% (MAE), respectively. Of the two configurations, the 8-channel input exhibited better prediction accuracy and convergence characteristics. As the number of training epochs increased, the errors of both configurations gradually decreased. However, the 8-channel model achieved stable convergence after approximately 300 epochs, while the 6-channel model required approximately 400 epochs and exhibited more pronounced fluctuations in the early stages of training. These results indicate that physics-aware features incorporating angular periodic encoding can strengthen the relationship between spatial state information and physical quantities and enhance the representation capability of the input features, thereby improving model training efficiency and prediction performance.

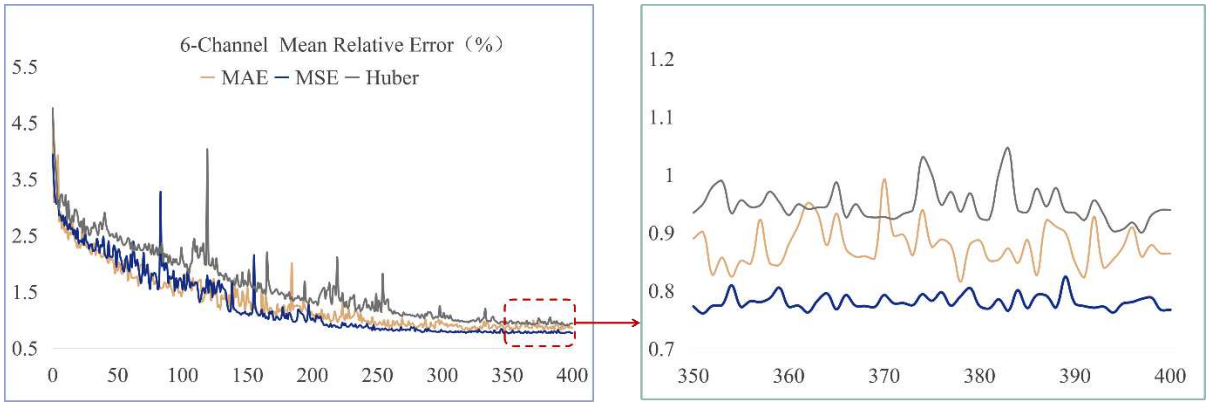

Fig. 15. Mean relative error curves for the 6-channel input.

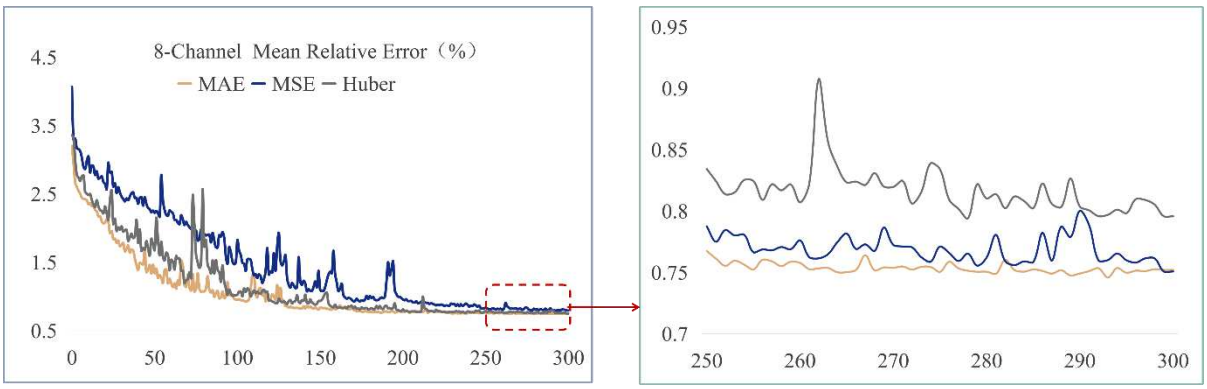

Fig. 16. Mean relative error curves for the 8-channel input.

Analysis of the Impact of CBAM on the Generalization Performance of E_{in} Response Prediction

Table 6 Effect of the CBAM Module on the Generalization Performance of Ein Response Prediction

Model	Mean Relative Error
3D U-Net	8.871%
3D CBAM U-Net	1.523%

To further investigate the role of the attention mechanism in electromagnetic prediction tasks, the baseline 3D U-Net and 3D CBAM U-Net models trained on the SAR_{10g} prediction task were directly applied to the E_{in} prediction task for comparison. The experimental results show that the baseline 3D U-Net exhibited a significant performance degradation, with a mean relative error of 8.871%. In contrast, the 3D U-Net model incorporating the CBAM module reduced the error to 1.523%, as shown in Table 6. These results indicate that the CBAM module enables the network to focus on regions with high spatial gradients in complex electromagnetic environments through channel and spatial attention mechanisms, thereby enhancing the model's ability to extract features of physical quantities and improving prediction accuracy.

Analysis of the Prediction Performance of 3D CBAM U-Net for Electromagnetic Exposure in the Human Head

In the SAR_{10g} prediction task, the model consistently achieved high fitting accuracy across different positions, with $R^2 > 0.948$ and 3D-SSIM > 0.940. Furthermore, when the trained network was generalized to the E_{in} prediction task, high prediction accuracy was achieved across all test conditions, with $R^2 > 0.941$ and 3D-SSIM > 0.926. These results demonstrate that the network can not only accurately predict SAR_{10g} values but also effectively extract high-gradient features across different physical quantities, exhibiting high generalization capability and fitting accuracy. In particular, the best overall prediction performance was achieved at r=10 mm, φ=300°, and θ=90°, with R^2 values of 0.991 and 0.988 for SAR_{10g} and E_{in}, respectively, and 3D-SSIM values exceeding 0.970 for both, as shown in Table 7 and Table 8.

Table 7 Prediction Performance Metrics for SAR_{10g} under Different Position Combinations

Position Combinations (r, φ, θ)	MAE	RMSE	R^2	3D-SSIM
10mm, 60°, 90°	0.212	0.391	0.950	0.940
10mm, 90°, 0°	0.190	0.489	0.948	0.968
10mm, 300°, 90°	0.169	0.307	0.991	0.974

Table 8 Prediction Performance Metrics for E_{in} under Different Position Combinations

Position Combinations (r, φ, θ)	MAE	RMSE	R^2	3D-SSIM
10mm, 60°, 90°	0.301	0.39	0.962	0.974
10mm, 90°, 0°	0.349	0.485	0.941	0.926
10mm, 300°, 90°	0.228	0.309	0.988	0.988

The 3D CBAM U-Net maintained high prediction accuracy, with a single prediction taking only 0.57 s. This represents an approximately 51-fold speedup compared with conventional finite element simulation. This computational advantage indicates that the proposed model can overcome the time limitations of conventional finite element methods in safety assessments of human head electromagnetic exposure under

different radiation source positions. As a result, computational efficiency is significantly improved. Notably, the predicted peak head SAR_{10g} values under all investigated positional conditions are well below the ICNIRP basic restriction of 2 W/kg for general public exposure. This indicates that head electromagnetic exposure remains within the safety limits under typical mobile phone usage scenarios. The proposed model enables rapid and reliable prediction of RF electromagnetic exposure in the human head at multiple positions. It also provides a useful reference for improving the efficiency of human exposure assessment.

Despite the significant advantages of the proposed framework, this study still has some limitations. First, the current dataset was generated using a single adult head model at a fixed frequency of 2.45 GHz. It does not account for anatomical differences among individuals of different ages and sexes, such as variations in tissue thickness and anatomical structure. Future work will incorporate more diverse anatomical models to improve the generalizability of the framework. Second, the simplified model and relatively limited sampling intervals may restrict its extrapolation capability for extreme positions beyond the training data distribution. Future studies will extend the framework to a wider range of positional scenarios and validate its predictions through electromagnetic simulations. These efforts are expected to improve its reliability in complex engineering applications.

Conclusions

To address the need for rapid prediction of electromagnetic exposure in the human head under typical mobile phone usage scenarios, this study proposes a 3D U-Net method that incorporates physics-aware spatial feature encoding as input and integrates the Convolutional Block Attention Module (CBAM). The method applies periodic encoding to spatial angles to construct two input configurations with eight and six channels, respectively. Each channel represents the geometric position of three-dimensional voxel data in space. Meanwhile, the CBAM module is integrated into the 3D U-Net to enhance the network's ability to extract features from key regions and improve its generalization performance. The network predicts SAR_{10g} and the E_{in} in the human head. The predicted results can be directly compared with the ICNIRP safety limits, providing a rapid prediction method for assessing the level of human electromagnetic exposure to mobile phone antennas.

The experimental results show that the network achieved a mean relative error as low as 0.748% for SAR_{10g} prediction in the head model. When the same network was applied to the E_{in} prediction task, the mean relative error was 1.523%. Compared with FEM simulation, a single prediction took only 0.57 s, achieving an approximately 51-fold speedup. These results demonstrate that the model maintains good prediction accuracy and generalization ability across different electromagnetic response tasks. This provides an efficient, accurate, and generalizable method for rapid prediction of electromagnetic exposure in the human head at multiple mobile phone positions.

References

[1] Imran, A., Li, C. & Zhang, Y. Analysis of SAR exposure in 3G, 4G, 5G and emerging 6G mobile communication technologies on the human head phantom model. *Discover Electronics* **2**, 100 (2025). https://doi.org/10.1007/s44291-025-00143-1.

[2] United Nations Environment Programme (UNEP). *Frontiers 2022: Noise, Blazes and Mismatches – Emerging Environmental Issues*. (United Nations, 2022). https://www.unep.org/resources/frontiers-2022-noise-blazes-and-mismatches.

[3] International Commission on Non-Ionizing Radiation Protection. Guidelines for limiting exposure to electromagnetic fields (100 kHz to 300 GHz). *Health Phys.* **118**, 483–524 (2020).

[4] IEEE. *IEEE C95.1-2019, Standard for Safety Levels with Respect to Human Exposure to Electric, Magnetic, and Electromagnetic Fields, 0 Hz to 300 GHz*. (IEEE, 2019).

[5] National People's Congress of the People's Republic of China. *Ecological and Environmental Code of the People's Republic of China*. (2026).

[6] Los Andes. Creció el uso del celular en el Mundo a nivel récord y América Latina lidera el alza. https://www.losandes.com.ar/tecno/crecio-el-uso-del-celular-el-mundo-nivel-record-y-america-latina-lidera-el-alza-n6002489 (2026).

[7] Fernandez, M., Espinosa, H. G., Thiel, D. V. & Arrinda, A. Wearable slot antenna at 2.45 GHz for off-body radiation: analysis of efficiency, frequency shift, and body absorption. *Bioelectromagnetics* **39**, 25–34 (2018). https://doi.org/10.1002/bem.22081.

[8] Jemaludin, N. H. et al. A comprehensive review on MIMO antennas for 5G smartphones: mutual coupling techniques, comparative studies, SAR analysis, and future directions. *Results Eng.* **23**, 102712 (2024). https://doi.org/10.1016/j.rineng.2024.102712.

[9] Ben Ishai, P., Davis, D., Taylor, H. & Birnbaum, L. Problems in evaluating the health impacts of radio frequency radiation. *Environ. Res.* **243**, 115038 (2024). https://doi.org/10.1016/j.envres.2022.115038.

[10] Bhargava, D., Rattanadecho, P. & Wessapan, T. The effect of metal objects on the SAR and temperature increase in the human head exposed to dipole antenna (numerical analysis). *Case Stud. Therm. Eng.* **22**, 100789 (2020). https://doi.org/10.1016/j.csite.2020.100789.

[11] Jalilian, H. et al. Personal radio frequency electromagnetic field exposure among Swiss adolescents in the 5G era. *Environ. Res.* **304**, 124775 (2026). https://doi.org/10.1016/j.envres.2026.124775.

[12] Röösli, M. et al. Mortality from neurodegenerative disease and exposure to extremely low-frequency magnetic fields: 31 years of observations on Swiss railway employees. *Neuroepidemiology* **28**, 197–206 (2007). https://doi.org/10.1159/000108111.

[13] Pei, Y. J. et al. High-efficiency computation for electromagnetic forming process: an explicit-implicit GPU approach. *iScience* **27**, 108735 (2024). https://doi.org/10.1016/j.isci.2023.108735.

[14] Ng, C.-K. et al. Electromagnetic modeling of human body using high performance computing. *Physics Procedia* **90**, 107–114 (2017). https://doi.org/10.1016/j.phpro.2017.09.033.

[15] Hirata, A. et al. Model variability in assessment of human exposure to radiofrequency fields. *IEEE J. Microw.* **6**, 502–518 (2025). https://doi.org/10.1109/JMW.2025.3628902.

[16] Guan, Z., Zhao, P., Wang, X. & Wang, G. Modeling radio-frequency devices based on deep learning technique. *Electronics* **10**, 1710 (2021). https://doi.org/10.3390/electronics10141710.

[17] Tang, W. et al. Study on a Poisson's equation solver based on deep learning technique. In *2017 IEEE Electrical Design of Advanced Packaging and Systems Symposium (EDAPS)*, 1–3 (IEEE, 2017). https://doi.org/10.1109/EDAPS.2017.8277017.

[18] Khan, M. R., Zekios, C. L., Bhardwaj, S. & Georgakopoulos, S. V. A deep learning convolutional neural network for antenna near-field prediction and surrogate modeling. *IEEE Access* **12**, 39737–39747 (2024). https://doi.org/10.1109/ACCESS.2024.3377219.

[19] Manassas, A., Delidimitriou, S., Wiart, J. & Samaras, T. Predicting electromagnetic field exposure using artificial intelligence methods. *IEEE Access* **13**, 79832–79844 (2025). https://doi.org/10.1109/ACCESS.2025.3566641.

[20] Chikha, W. B., Wang, S. & Wiart, J. An extrapolation approach for RF-EMF exposure prediction in an urban area using artificial neural network. *IEEE Access* **11**, 52686–52694 (2023). https://doi.org/10.1109/ACCESS.2023.3280125.

[21] Cao, M. et al. Field reconstruction for high-frequency electromagnetic exposure assessment based on deep learning. *IEEE Trans. Antennas Propag.* **74**, 6954–6966 (2026). https://doi.org/10.1109/TAP.2026.3681071.

[22] Gokyar, S., Zhao, C. Y., Ma, S. J. & Wang, D. J. J. Deep learning-based local SAR prediction using B1 maps and structural MRI of the head for parallel transmission at 7 T. *Magn. Reson. Med.* **90**, 2524–2538 (2023). https://doi.org/10.1002/mrm.29797.

[23] Berger, T. A. et al. Comprehensive evaluation of U-Net based transcranial magnetic stimulation electric field estimations. *Sci. Rep.* **15**, 12204 (2025). https://doi.org/10.1038/s41598-025-95767-4.

[24] Gandhi, O. P., Lazzi, G. & Furse, C. M. Electromagnetic absorption in the human head and neck for mobile telephones at

835 and 1900 MHz. *IEEE Trans. Microw. Theory Techn.* **44**, 1884–1897 (1996). https://doi.org/10.1109/22.539947.

[25] Meier, K. et al. The dependence of electromagnetic energy absorption upon human-head modeling at 1800 MHz. *IEEE Trans. Microw. Theory Techn.* **45**, 2058–2062 (1997). https://doi.org/10.1109/22.644237.

[26] Ronneberger, O., Fischer, P. & Brox, T. U-Net: convolutional networks for biomedical image segmentation. In *Medical Image Computing and Computer-Assisted Intervention – MICCAI 2015*, 234–241 (Springer, 2015). https://doi.org/10.1007/978-3-319-24574-4_28.

[27] Woo, S., Park, J., Lee, J.-Y. & Kweon, I. S. CBAM: convolutional block attention module. In *Proceedings of the European Conference on Computer Vision (ECCV)*, 3–19 (2018). https://doi.org/10.48550/arXiv.1807.06521.

[28] Schmid, G., Neubauer, G. & Mazal, P. R. Dielectric properties of human brain tissue measured less than 10 h postmortem at frequencies from 800 to 2450 MHz. *Bioelectromagnetics* **24**, 423–430 (2003). https://doi.org/10.1002/bem.10123.

[29] Vallejo, J. L., Recas, J., del Valle, P. G. & Ayala, J. L. Accurate human tissue characterization for energy-efficient wireless on-body communications. *Sensors* **13**, 7546–7569 (2013). https://doi.org/10.3390/s130607546.

[30] Ji, R., Lu, C. & Zhong, J. Dynamic differencing-based hybrid network for improved 3D skeleton-based motion prediction. *AI* **5**, 2897–2913 (2024). https://doi.org/10.3390/ai5040139.

[31] Duran, G. C. et al. Electrical impedance tomography image reconstruction using convolutional neural network with periodic padding. *IFAC-PapersOnLine* **54**, 418–423 (2021). https://doi.org/10.1016/j.ifacol.2021.10.292.

[32] Alsallakh, B., Kokhlikyan, N., Miglani, V., Yuan, J. & Reblitz-Richardson, O. Mind the pad – CNNs can develop blind spots. In *International Conference on Learning Representations* (2021). https://openreview.net/forum?id=m1CD7tPubNy.

[33] Terven, J. et al. A comprehensive survey of loss functions and metrics in deep learning. *Artif. Intell. Rev.* **58**, 195 (2025). https://doi.org/10.1007/s10462-025-11198-7.